Analytical model for solar irradiance near a planar vertical diffuse reflector – Formulation, validation, and simulations[1]

Matthew Boyd

National Institute of Standards and Technology (NIST), Gaithersburg, MD, USA

Abstract

An analytical model is formulated for the irradiance on a surface (collector) with a rear (opposite the sun) planar vertical diffuse reflector, as is common for a lower roof on a multi-story building. The vast majority of research on solar reflectors has been for specular, or mirror, reflectors, with any diffuse reflections modeled about the specular reflection angle. This model is capable of calculating incident and reflected direct, diffuse, and ground-reflected radiation using components borrowed from the Hay, Davies, Klucher, Reindl (HDKR) irradiance model, and is easily implemented in any computation programming software capable of numeric integration. The model accounts for reflector edge effects and shading of diffuse and ground-reflected radiation by the reflector, but it does not account for shading of beam radiation by the reflector.

The model shows good overall agreement with experimental tests, and is three percentage points more accurate than a standard radiation model for tilted surfaces. The model indicates that a planar vertical diffuse reflector increases the irradiance at high clearness indices and low reflector incidence angles, and decreases the irradiance otherwise. Increasing the reflector height and decreasing the collector pitch and distance between the collector and reflector increases the irradiance during clear periods, but decreases the irradiance, to a lesser absolute extent, during cloudy periods. Annual simulations show a gain in winter insolation and a loss in summer insolation for an average collector/reflector, with an increase in annual insolation for collectors near high albedo reflectors.

Keywords: Solar irradiance model; Diffuse reflector; Experimental validation; Annual simulation

1. Introduction

Many of the available equatorial facing roofs ideal for installing solar collectors, either hot water or photovoltaic, are adjacent to rear (opposite the sun) vertical walls. These walls, depending on their properties, can reflect irradiance onto collectors and/or shade the collectors from diffuse and beam radiation coming from behind the wall. The test bed used for this research, a mock-up of a pitched residential roof in front of a light-colored brick wall, as shown in Figure 1, was originally constructed for measuring and

Figure 1: Building-Integrated Photovoltaic (BIPV) test bed and rear wall used for model validation.

[1] Boyd, M., 2013. Analytical model for solar irradiance near a planar vertical diffuse reflector – Formulation, validation, and simulations. Solar Energy 91, 79–92. http://dx.doi.org/10.1016/j.solener.2013.01.015

Nomenclature

A_i	anisotropy index in HDKR model, -, or the area of the *i*th reflecting surface on the reflector, m^2
A_c	area of collector, m^2
BIPV	building-integrated photovoltaics
BORCAL	Broadband Outdoor Radiometer Calibration
C_{ISO}	ISO 9847 calibration coefficient, -
$F_{c\text{-}g}$	radiation view factor from the collector to the ground, -
$F_{c\text{-}hz}$	radiation view factor from collector to the area of the sky above the horizon, -
$F_{c\text{-}i}$	radiation view factor from the collector to the *i*th reflecting surface on the reflector, -
$F_{c\text{-}r}$	radiation view factor from the collector to the entire reflector (both reflecting and non-reflecting surfaces), -
$F_{c\text{-}s}$	radiation view factor from the collector to the sky, -
$F_{i\text{-}j}$	radiation view factor from the *i*th surface to the *j*th surface, -
f	modulating factor in HDKR model, -
G	total horizontal irradiance, W/m^2, or the integral component in the collector to reflector view factor equation, m^2
G_b	beam (direct) horizontal radiation, W/m^2
G_{bn}	beam (direct) normal radiation, W/m^2
G_d	diffuse horizontal irradiance, W/m^2
$G_{d,cs}$	circumsolar diffuse horizontal irradiance, W/m^2
$G_{d,hz}$	horizon brightening diffuse horizontal irradiance, W/m^2
$G_{d,iso}$	isotropic diffuse horizontal irradiance, W/m^2
G_i	total irradiance on the *i*th reflecting surface, W/m^2
G_o	extraterrestrial horizontal radiation, W/m^2
G_{on}	extraterrestrial normal radiation, W/m^2
G_r	total irradiance on the reflector, W/m^2
G_T	total irradiance on a tilted surface, W/m^2
$G_{T,aug}$	augmented total irradiance on a tilted surface, W/m^2
$G_{T,HDKR}$	total irradiance on a tilted surface modeled with the HDKR radiation model, W/m^2
GUM	*Guide to the Expression of Uncertainty in Measurement*
HDKR	Hay, Davies, Klucher, Reindl radiation model
H_r	reflector height, m
IECC	International Energy Conservation Code
IR	infrared radiation
ISO	International Organization for Standardization
k	coverage factor, -
k_T	clearness index, -
MBE	mean bias error
N	north
N_{df}	number of degrees of freedom
NIST	National Institute of Standards and Technology
NREL	National Renewable Energy Laboratory
n	number of data points
net-IR	net infrared radiation ($IR_{in} - IR_{out}$), W/m^2
R_{net}	IR responsivity, μV/W/m^2
RSS	root-sum-square
SER	standard error of regression
TMY3	typical meteorological year data, third set
U	expanded uncertainty
V	voltage, μV
W	west
W_{net}	net infrared radiation, W/m^2
x_i	*i*th measured data value, or the *i*th *x*-coordinate of the collector area, m
$Y_{T,aug}$	modeled total annual augmented insolation on a tilted surface, W·h/m^2
$Y_{T,HDKR}$	total annual insolation on a tilted surface modeled with the HDKR radiation model, W·h/m^2
$y_{i\,[j]}$	*i*th modeled data value, or the *j*th *y*-coordinate of the collector area, m

Greek symbols

α	*angle between the collector and reflector,* °
α_s	solar altitude angle, °
β	pitch, slope, or tilt, °
γ_s	solar azimuth angle (0° = south) , °
δ	declination, °
η_k	*k*th η-coordinate of the reflector area, m
θ	incidence angle, °
θ_z	solar zenith angle, °
ξ_l	*l*th ξ-coordinate of the reflector area, m
ρ_g	albedo of the ground, -
ρ_i	albedo of *i*th surface, -
ρ_r	albedo of reflector, -
ϕ	latitude, °
ω	hour angle, °

Subscripts

aug	augmented
b	beam
c	collector
cs	circumsolar
d	diffuse
df	degrees of freedom
g	ground
HDKR	modeled with HDKR radiation model
hz	horizon brightening
i	data point index
iso	isotropic
j	data point index
n	normal orientation
net	input – output
no bias	mean bias subtracted
o	extraterrestrial
r	reflector
rel	relative
s	sky, or solar
T	tilted

R	shortwave responsivity, μV/W/m^2	*Symbols*	
R^2	coefficient of determination	:	in, (e.g., 6:12 = "six in twelve", relating to the rise and run, respectively, in pitch)
R_b	ratio of beam (direct) radiation on a tilted surface to that on a horizontal surface	-	to, relating to radiation view factors
RMSE	root-mean-square error		

characterizing building- integrated photovoltaic (BIPV) arrays. Initial analysis of the data during sunny periods revealed higher than expected generation and a spot check of irradiances at solar noon using a pyranometer indicated that irradiances were as much as 10 % higher for some roof locations relative to the permanent pyranometer installations. These variations in the expected outputs provided the impetus for this research.

Most prior research modeling solar reflectors has been for specular (mirror) reflectors (McDaniels et al., 1975; Grassie and Sheridan, 1977; Larson, 1979, 1980; Chiam, 1981, 1982; Perers and Karlsson, 1993; Bollentin and Wilk, 1995), which are used to actively concentrate solar irradiance on collectors, but very little research is applicable to passive diffuse reflectors like typical exterior walls. The model by Grimmer et al. (1978) incorporates "directed diffuse" reflections from largely specular reflectors that are centered about the specular reflection angle, but this model does not consider diffuse sky and ground reflected radiation, nor its respective directional distribution and shading by the reflector.

Diffuse reflections are incorporated into interior daylighting models in building simulation programs like EnergyPlus (Crawley et al., 2000) and DOE-2 (Winkelmann et al., 1993), but these models assume that the rooms behave like integrating spheres, resulting in uniform reflected illuminance on the interior surfaces (US Department of Energy, 2012; Winkelmann, 1983). Another building simulation program, BESim, which is not publically available (Duc Hien and Chirarattananon, 2009), models diffuse reflections from arbitrary surfaces using a numerical method of calculating view factors between triangular subdivisions of these surfaces (Hein and Chirarattananon, 2005). BESim does not appear to incorporate the different areas of an anisotropic sky into this view factor calculation method, so it may only be applicable to enclosed (interior) spaces or between defined surfaces.

This paper presents the theoretical methods used to model irradiance near a finite length planar vertical diffuse reflector and the experimental methods used to measure high-accuracy shortwave solar irradiance for validating the model. The impact of a reflector on collector irradiance is quantified for different sky clearness indices, reflector incidence angles, reflectivities, and heights and collector pitches. The cumulative effect over a representative year in different climate zones, differentiating between winter and summer behavior, is also evaluated.

2. Model

2.1. Formulation

The basic form chosen for the model is:

$$G_{T,aug} = G_b R_b + G_{d,iso} F_{c-s} + G_{d,cs} R_b + G_{d,hz} F_{c-hz} + \sum_i G_i \rho_i F_{c-i} \tag{1}$$

where R_b is the ratio of the beam radiation on the pitched collector to that on a horizontal surface (Duffie and Beckman, 2006), defined by:

$$R_b = \frac{\cos(\phi-\beta)\cos\delta\cos\omega + \sin(\phi-\beta)\sin\delta}{\cos\phi\cos\delta\cos\omega + \sin\phi\sin\delta} \tag{2}$$

$G_{T,aug}$ is the total augmented irradiance on the tilted (pitched) collector, G_b is the beam, or direct horizontal radiation, $G_{d,iso}$ is the isotropic diffuse horizontal irradiance, F_{c-s} is the radiation view factor from the collector to the sky, $G_{d,cs}$ is the circumsolar diffuse horizontal irradiance, $G_{d,hz}$ is the horizon brightening diffuse horizontal irradiance, F_{c-hz} is the radiation view factor from the collector to the area of the sky above the horizon, G_i is the total irradiance on the ith reflecting surface, ρ_i is the diffuse reflectivity, or albedo, of that surface, F_{c-i} is the radiation view factor from the collector to that surface (Duffie and Beckman, 2006), ϕ is the latitude, β is the pitch of the collector, δ is the declination, and ω is the hour angle.

The radiation component terms from the Hay, Davies, Klucher, and Reindl (HDKR) irradiance model (minus the view factors) (Reindl et al., 1990) are substituted into equation (1) to make:

$$G_{T,aug} = G_b R_b + G_d (1-A_i) F_{c-s} + G_d A_i R_b + G_d (1-A_i) f \sin^3\left(\frac{\beta}{2}\right) F_{c-hz} + G\rho_g F_{c-g} + \sum_i G_r \rho_r F_{c-i} \tag{3}$$

Equation (3) is factored, with the radiation view factor F_{c-hz} set equal to F_{c-s}, as is consistent with the HDKR model, resulting in:

$$G_{T,aug} = \left(G_b + G_d A_i\right) R_b + G_d \left(1 - A_i\right) F_{c-s} \left[1 + f \sin^3\left(\frac{\beta}{2}\right)\right] + G \rho_g F_{c-g} + \sum_i G_r \rho_r F_{c-i} \quad (4)$$

where:

$$G_b = G_{bn} \cos\theta_z \quad (5)$$

$$A_i = \frac{G_{bn}}{G_{on}} = \frac{G_b}{G_o} \quad (6)$$

$$f = \sqrt{\frac{G_b}{G}} \quad (7)$$

A_i is the anisotropy index, G_d is the (total) diffuse horizontal irradiance, f is a modulating factor, G is the total, or sum of the beam and diffuse horizontal irradiance (equal to the total irradiance on the ground), ρ_g is the albedo of the ground, $F_{c\text{-}g}$ is the view factor from the collector to the ground, G_r is the total irradiance on the reflector, ρ_r is the albedo of the reflector, $F_{c\text{-}i}$ is the view factor from the collector to the *i*th reflecting surface on the reflector, G_{bn} is the beam radiation normal to the sun, θ_z is the solar zenith angle, G_{on} is the extraterrestrial radiation normal to the sun, and G_o is the extraterrestrial horizontal radiation. The irradiance on the reflector is modeled in this study using the HDKR model (Reindl, 1990).

The HDKR model is chosen over other anisotropic transposition models because it is one of the most accurate (Loutzenhiser et al., 2007), if not the most accurate (Padovan and Del Col, 2010) model for tilted total irradiance available, but also because it is notably more accurate at modeling the irradiance on a vertical south-facing surface (or reflector) (Gueymard, 2009). The HDKR model also has fewer terms than other comparably accurate models, making it simpler to implement and modify. Regardless, the radiation component terms or vertical irradiance in this augmented model can be modeled using other irradiance models if desired.

The view factors $F_{c\text{-}i}$ that are from the collector, or any rectangular area on the collector, to the *i*th reflecting surfaces are very large integrals (Howell, 2012) defined according to and the following equations:

$$F_{c-i} = \frac{1}{A_c} \sum_{i=1}^{2} \sum_{j=1}^{2} \sum_{k=1}^{2} \left[\left(-1\right)^{(i+j+k+l)} G\left(x_i, y_j, \eta_k, \xi_l\right)\right] \quad (8)$$

where A_1 is the collector area, x_i and y_j are the *i*th coordinates of the collector area in the *xy* plane, η_k and ξ_l are the *i*th coordinates of the reflector area in the $\eta\xi$ plane, and G is defined as:

$$G = -\frac{(\eta - y)\sin^2\alpha}{2\pi} \int_\xi \left(\frac{(x - \xi\cos\alpha)\cos\alpha - \xi\sin^2\alpha}{\left(x^2 - 2x\xi\cos\alpha + \xi^2\right)^{1/2}\sin^2\alpha} \tan^{-1}\left[\frac{\eta - y}{\left(x^2 - 2x\xi\cos\alpha + \xi^2\right)^{1/2}}\right] + \frac{\cos\alpha}{(\eta - y)\sin^2\alpha}\left\{\left[\xi^2\sin^2\alpha + (\eta - y)^2\right]^{1/2} \tan^{-1}\frac{x - \xi\cos\alpha}{\left[\xi^2\sin^2\alpha + (\eta - y)^2\right]^{1/2}} - \xi\sin\alpha\tan^{-1}\left(\frac{x - \xi\cos\alpha}{\sin\alpha}\right)\right\} + \frac{\xi}{2(\eta - y)}\ln\left[\frac{x^2 - 2x\xi\cos\alpha + \xi^2 + (\eta - y)^2}{x^2 - 2x\xi\cos\alpha + \xi^2}\right]\right) d\xi \quad (9)$$

where α is the angle between the *xy* and $\eta\xi$ plane. These integrals must be solved numerically, and are calculated here using the *F3D_30* internal function in EES[1] (Klein, 2012). Another similar function for MATLAB (2010) is also known to exist (Lauzier, 2004), but the equations can be implemented in any computational software capable of numeric integration. Three view factors are calculated for the reflector in this study, one for each of the sections of the brick wall: above, below, and to the right of the metal louvers, as can be seen in Figure 1, with the irradiance on, and albedo of these sections assumed to be equal. The black trim at the top of the wall and the louvers, since they tilt up, are assumed to reflect no radiation onto the roof (collector).

The view factors $F_{c\text{-}g}$ (Howell, 2012) and $F_{c\text{-}s}$ are:

$$F_{c-g} = \frac{\left(1 - \cos\beta\right)}{2} \quad (10)$$

$$F_{c-s} = 1 - F_{c-g} - F_{c-r} \quad (11)$$

where $F_{c\text{-}g}$ is equal to that in the HDKR model, $F_{c\text{-}s}$ is calculated using the view factor summation rule ($\sum_j F_{i-j} = 1$), and $F_{c\text{-}r}$ is the view factor between the collector and the entire "reflector," not just the surfaces of the reflector that are reflecting.

2.2. Assumptions and Limitations

The model is applicable to any reflector/collector azimuth orientation, but it does not account for shading of beam radiation by the reflector(s); therefore, for this test bed which faces the equator in the northern hemisphere, the model is only valid for solar azimuth angles between ±90° (0° = south), when there is no beam shading.

The model assumes, by the use of view factors $F_{c\text{-}i}$ and $F_{c\text{-}r}$, that the reflectors are gray Lambertian reflectors, which have radiance independent of wavelength and angle of reflection. This is generally a good assumption, but the reflector may be reflecting more of its irradiance at higher reflection angles since it has a rough texture (Oren and Nayar, 1994), or if it exhibits some specular reflectivity.

---

[1] In no case does an identification of trade names, company names, or commercial products imply recommendation or endorsement by the National Institute of Standards and Technology, nor does it imply that the products are necessarily the best available for the purpose.

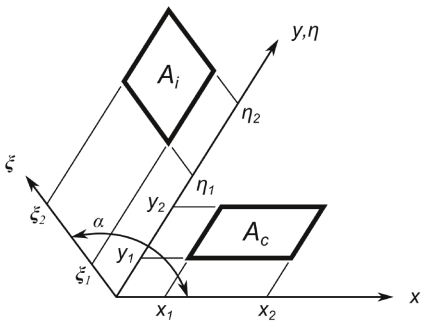

Figure 2: Diagram of the view factor from the collector, or any rectangular area on the collector, to the *i*th reflecting surface on the reflector.

Regarding the model validation, the ground albedo (ρ_g) is assumed to be 0.1 (Hansen, 1993), which includes the albedo of the collector (reflecting onto the reflector). The reflector (wall) is also assumed to not emit any radiation in the spectral ranges of the shortwave radiometers used to measure the collector irradiance. This assumption is supported by a calculation showing that only 0.03 % of the maximum radiation emitted by a reflector, modeled as an 80 °C blackbody, is within the radiometer spectral range of 285 nm to 2800 nm.

3. Experimental Validation

3.1. Test Bed and Instrumentation

The test bed used for this research is located on the campus of the National Institute of Standards and Technology (NIST) in Gaithersburg, Maryland (39.14 °N, -77.22 °W). It is a nominal 4:12 (18.4°) pitched roof facing true south, having a 9.32 m by 3.45 m (30.6 ft by 11.3 ft) roof deck, with a vertical light-colored brick wall rising 3.3 m (10.8 ft) above the back of the roof. The east edge of the roof is nearly adjacent to the east edge of the wall, with the roof extending 10 cm (4 in.) beyond the wall. Aluminum louvers 0.63 m (2.1 ft) tall are 1.47 m (4.8 ft) above the roof and 1.73 m (5.7 ft) from the east edge of the wall. Black-anodized aluminum flashing 0.25 m (0.8 ft) wide borders the top of the wall.

The original purpose of this test bed was to measure the side-by-side performance of building-integrated photovoltaics (BIPV). Six different arrays are integrated into the roof, with pyranometer mounts installed on the far east end nearer to the south. The array pitches range from 11° to 17°, with an average pitch near 12°. These differences are due to how the front edges of the modules in the individual arrays are mounted onto battens and flashing.

Measurement locations for model validation were based on initial modeling of the roof. Results for a representative sunny day, shown in Figure 3, indicate higher irradiance gradients near the east end of the roof at the edge of the wall, and relatively flat gradients in the east/west direction away from the edge of the wall. (Note: for a homogenous wall without the metal louvers and trim, the steep gradients on the east edge of the roof extend 1 m to 2 m (3.3 ft to 6.6 ft) further west and there is almost an additional one percentage point increase in irradiance.) Six measurement locations were chosen, as shown in the plot, that span the entire expected in-plane irradiance ranges, include all boundary effects, and are in a symmetric pattern that allows for simple comparisons.

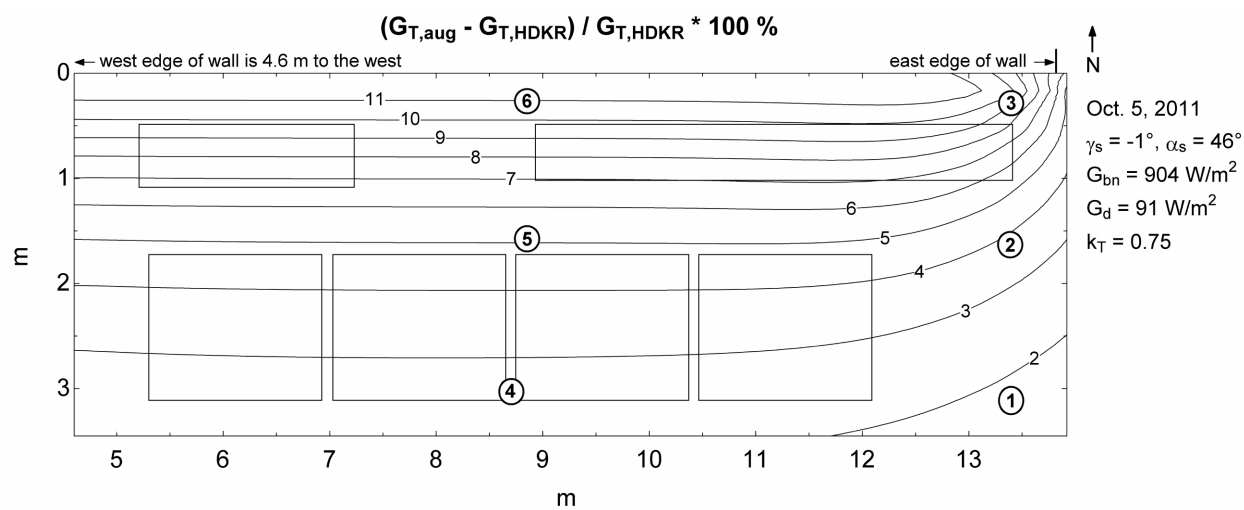

Figure 3: Modeled spatial irradiance distribution at solar noon – percent difference relative to no wall being present (using HDKR model). Horizontal and vertical axes are distances measured from the wall in the plane of the roof and from the west edge of the wall, respectively. Rectangular outlines of the original BIPV arrays and the current test pyranometers are shown, along with the date and measured values used as inputs to the models, the solar azimuth (γ_s) and altitude angles (α_s), and the clearness index (k_T). Original test pyranometers were located between test positions 1 and 2.

The beam normal radiation (G_{bn}) and diffuse horizontal irradiance (G_d) used in the model are measured using pyrheliometers and black and white pyranometers, respectively, mounted on a solar tracker located above the wall on an upper flat roof in full view of the sky. The accuracy of the solar tracker was confirmed by frequent checks during the tests to be within 0.3°, which is well within the needed accuracy of 0.75° for getting a full response from these pyrheliometers (Kipp and Zonen, 2008), and well within that needed to keep the shading disks centered over the diffuse-measuring pyranometers. Two of each instrument are deployed on the tracker, and the respective averages are used in an effort to reduce the uncertainty. All four instruments are calibrated by the National Renewable Energy Laboratory (NREL) according to their Broadband Outdoor Radiometer Calibration (BORCAL) procedure (Myers, 2002). The instruments were deployed only briefly after their calibrations and prior to these tests so any drift from the calibration values is assumed to be negligible. The 45° calibration responsivities are used for the pyrheliometers and the *composite* responsivities are used for the black and white pyranometers; neither radiometer types are affected by net-IR ($IR_{in} - IR_{out}$).

The tilted total irradiances (G_T) are measured using *secondary standard* thermopile pyranometers with all-black sensors mounted in the locations shown in Figure 3, at the average roof pitch of 12° ± 0.5°, facing true south, and with connectors facing north, away from the equator. Another pyranometer of the same type is located above the wall near the solar tracker in an identical configuration. These pyranometers are calibrated by NREL according to their BORCAL procedure and all were also deployed only briefly after their calibrations, so any drift from their calibrations is assumed to be negligible. The net-IR corrected, incidence angle dependent responsivities from the calibrations (in units of μV/W/m^2) are provided every two degrees and interpolated into 19 to 23rd order polynomials. The estimated IR (longwave) responsivities of the pyranometers are also provided with these calibration results. The pyranometer readings are corrected for offsets generated by net-IR using net-IR measurements from a pyrgeometer, which was calibrated outdoors at NREL. A single test with this pyrgeometer showed that the difference in in-plane net-IR between various locations on the pitched roof and on the above horizontal roof was on average 7 W/m^2 (8 %) and peaked at 22 W/m^2 (27 %), with the larger (more negative) measurements generally on the pitched roof. This difference is deemed an acceptable uncertainty due to the low sensitivity of the pyranometer readings to net-IR. Therefore, a single pyrgeometer was installed in a horizontal position near the solar tracker and its net-IR readings are used to correct all the tilted pyranometer readings according to:

$$G_T = \frac{V - W_{net} R_{net}}{R(\theta)} \tag{12}$$

where G_T is the measured tilted total horizontal irradiance, V is the voltage signal from the pyranometer, W_{net} is the net-IR radiation measured using a pyrgeometer, R_{net} is the IR (longwave) responsivity of the pyranometer, and $R(\theta)$ is the (shortwave) responsivity of the pyranometer as a function of the incidence angle.

In addition to the BORCAL calibrations, the pyranometers were further calibrated on the upper roof in a horizontal position during stable cloudless sky conditions at incidence angles less than 75° using the International Organization for Standardization (ISO) 9847 standard procedure (ISO, 1992). This additional calibration is intended to maximize the precision between the total and combined beam and diffuse measurements. The pyranometer readings are first corrected using equation (12) and these irradiance values are used instead of the voltages as specified by the standard. The combined beam and diffuse measurements using the respective averages from the redundant tracking instruments are used as the reference irradiance values. The complete calibration function for the pyranometers is therefore:

$$G_T = C_{ISO} \frac{V - W_{net} R_{net}}{R(\theta)} \tag{13}$$

where C_{ISO} is the ISO 9847 calibration coefficient. The calibration coefficients for the different pyranometers range from 0.993 to 1.004, or a maximum correction of only 0.7 %.

The total hemispherical reflectivity (albedo) of the wall (ρ_r in equation (4)) is the ratio of the reflected radiation from the wall to the total irradiance on the wall. This value was measured by mounting two pyranometers, back to back, in front of the *east* facing wall. One pyranometer faced the wall, the other faced away. For this test only, the *composite* net-IR corrected responsivities from the BORCAL calibrations are used for both pyranometers, and an approximate average net-IR value of -100 W/m^2, calculated from previous long-term horizontal measurements at NIST, is used in the calibration equations. The calculated albedo is 0.45 with a U_{95} uncertainty of ±0.01 for incidence angles 16° to 87°. This value is very near that of dry sand (0.40) (Hansen, 1993), which has a similar color and texture, giving further confidence to the experimental result.

3.2. Data Acquisition and Filtering

All instruments are connected via grounded, shielded, twisted-pair cabling to a 6-1/2 digit multiplexed voltmeter with a greater than 10 GΩ impedance that measures and stores instantaneous readings every 10 s. Measurements are made with an integration time of 10 power line cycles, or 0.17 s for the 60 Hz line power, with zero offsets measured and subtracted from each reading. All instruments were cleaned every morning using alcohol and optical cloths, and

compressed air was used to remove any remaining fibers. Fixed instrument tilts were checked every week and verified to be within ±0.5° of nominal.

Measurements were taken on relatively clear days between April 29 and July 25 during daylight periods when the solar azimuth angles were between ±90° (0° = south). These predominately clear days were chosen to minimize the errors associated with transients, differences from calibration conditions, and the generally higher uncertainties with diffuse modeling.

The data set is filtered by removing data measured at times when any of the instruments were cleaned or obstructed during periodic checks. Mild outliers in the data set are kept, but data are removed at times when there are extreme outliers associated with any of the instruments. Extreme outliers are defined as the model residuals that are three times the interquartile range beyond the upper and lower quartiles (NIST/SEMATECH, 2012). This data filtering is done to allow for more representative calculations of the mean bias and root-mean-squared modeling errors.

A total of 2.8% of the data points are removed due to outliers. The vast majority of these were measured after solar noon but at relatively low zenith angles, including for the measurement location above the wall. This coincides with when the tracker was typically checked for alignment and occasionally adjusted. Therefore, the majority of the outliers are likely from human obstruction of the solar tracking instruments. No other significant correlations with the residuals are observed.

3.3. Uncertainty

All uncertainties are calculated in accordance with the *Guide to the Expression of Uncertainty in Measurement* (GUM) (JCGM/WG 1, 2010), and specifically following the procedure outlined by Reda (2011) for shortwave solar radiometers. The Type A (statistical) uncertainties are from the standard error of regressions (SER) of the BORCAL responsivity regressions, the ISO calibrations, and the measured reflector (wall) albedo; calculated according to:

$$U = k\sqrt{\frac{1}{N_{df}}\sum_i \left(y_i - x_i\right)^2} \tag{14}$$

where U is the expanded uncertainty, k is the coverage factor, N_{df} is the number of degrees of freedom, which is the number of data points minus the number of fitted parameters, y_i is the ith fitted value, and x_i is the ith data point. For the BORCAL responsivity regressions, y_i is the value of the calculated regression at the ith incidence angle and x_i is the measured value. For the ISO calibrations, y_i is calibration factor at the ith measured data point, or the ratio of the combined measured reference irradiance to the measured pyranometer irradiance, and x_i is the single calibration factor as calculated according to the procedure. For the reflector albedo, a similar approach to the ISO calibrations is used, where x_i is the single averaged value. There are no Type A uncertainties associated with the pyranometer voltage signals as they are all measured instantaneously, minus meter integration times; therefore, all other uncertainties are Type B (non-statistical). The expanded uncertainties at a 95 % confidence level for the measured and calculated variables used in the pyranometer calibration equation (equation (13)) are listed in Table 1.

Table 1
Expanded uncertainties for the variables in the pyranometer calibration function.

	U_{95}
ISO Calibration (C_{ISO})	1 % to 2 %
Voltage (V)	0.04 % to 0.75 %
Net-IR (W_{net})[1]	16 % to 18 %
IR Responsivity (R_{net})[2]	20 %
Calculated Incidence Angle (θ)[3]	0.02°
Responsivity ($R(\theta)$) (*RSS* of components)	2.3 % to 4.5 %
Spectral Response[2]	{1 %}
Azimuth[2]	{1 %}
Tilt[4] (12°)	{0.2 %}
Nonlinearity[5]	{0.5 %}
Temperature Dependence[5]	{1 %}
Aging/Non-stability[5]	{0.2 %}
BORCAL Calibration[6]	{1.2 % to 1.5 %}
Responsivity Regression	{0.6 % to 3.8 %}
$0.02° \cdot \partial R_{max}/\partial\theta$ [7]	{0.12 % to 0.70 %}

[1] including estimated uncertainty from reflector emission and roof pitch
[2] Reda, 2011
[3] Pelletier, 2005 (implementation of equations in *Astronomical Algorithms* by Jean Meeus and corrected for atmospheric refraction)
[4] Duffie and Beckman, 2006
[5] instrument specifications
[6] average of AM and PM responsivities from BORCAL calibration data
[7] the sensitivity factor $\partial R_{max}/\partial\theta$ is the maximum derivative of the responsivity regression between 0° and 75°

3.4 Results

The model validation is performed according to a standard method proposed by Stein et al. (2010). The modeled versus measured values with associated measurement uncertainties and modeled minus measured residuals, for four of the six measurement locations are shown in Figure 4. The individual error bars in Figure 4a are not fully discernable, but do show the approximate bound of the measurement uncertainty. The agreement of the modeled with the measured values appears to be consistent over the full range of measurements, as shown in Figure 4a. There is no apparent trend in the daily modeling bias errors with time, as shown in Figure 4b; therefore, degradation of the measurement accuracy or change in the experimental setup is not significant. The residuals in Figure 4c also show an approximate normal distribution indicating that most are

random errors and the model is valid. The skew towards negative residuals near zero is expected because the irradiance, and therefore the magnitude of the residuals, is lower twice a day in the morning and evening, resulting in more low irradiance residuals. The skew does show, however, that the model is slightly underpredicting the irradiance at these times.

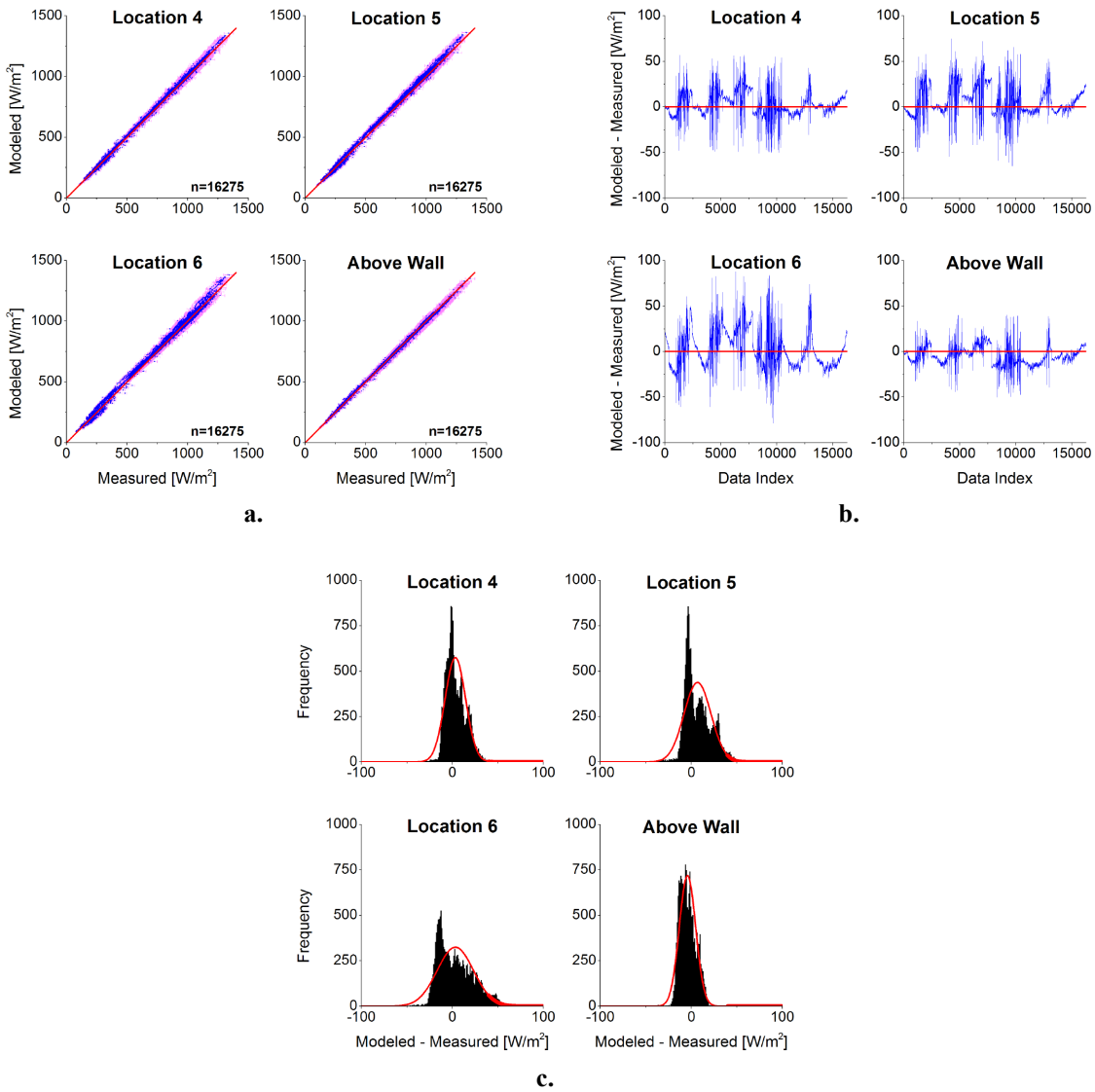

Figure 4: Modeled versus measured and modeled minus measured residuals for select locations in front of and above reflector. Error bars corresponding to U_{95} uncertainties for the measured values are included in *a* to show the approximate bound of the measurement errors.

In accordance to the aforementioned guides on uncertainty, the Type A and Type B standard measurement uncertainties are combined in quadrature (root-sum-square (RSS)) into a combined standard uncertainty and multiplied by a coverage factor. For a 95 % confidence level on the uncertainty, $k = 1.96$, taken from the Student's *t*-distribution for greater than 100, or effectively infinite residuals having a bell shaped distribution (NIST/SEMATECH, 2012). The uncertainties for four of the measurement locations are shown in Figure 4a, and the range and respective component uncertainties for all the locations are listed in Table 2.

Table 2
Maximum expanded uncertainties and respective component uncertainties of the pyranometer measurements.

Location	1	2	3	4	5	6	Above Wall
Type A (u_A) %	0.6	2.3	1.4	1.0	0.7	0.8	0.8
Type B (u_B) %	1.2	1.7	2.0	1.6	1.6	1.8	1.5
Combined (u_C) %	1.3	2.9	2.4	1.9	1.8	2.0	1.7
Expanded (U_{95}) % (k=1.96)	2.6	5.6	4.7	3.7	3.5	4.0	3.6

A relatively large fraction of the combined uncertainty is shown to be Type A, from the ISO 9847 calibration and the responsivity regression. The ISO 9847 calibration improves the precision between the pyranometers, but it also introduces additional uncertainty. A greater fraction of the Type A uncertainy, however, is from the responsivity regressions. The responsivities measured during the morning of the calibration (AM) and those measured during the afternoon (PM) do not always overlap at equal zenith angles, likely due to spectral or temperature changes during the calibration or an azimuth response from the pyranometer. The responsivity regression is fit to the average of the AM and PM values at each zenith angle, and the large uncertainty arises from calculating the standard error of regression (equation (14)) using the maximum difference between this regression and the respective AM and PM values.

The uncertainty in the *model* is calculated using:

$$MBE = \left[\frac{1}{n} \sum_{i=1}^{n} \left(y_i - x_i \right) \right] \tag{15}$$

$$RMSE_{rel,no\ bias} = \sqrt{\frac{1}{n} \sum_{i=1}^{n} \left(y_i - MBE - x_i \right)^2} \div \left[\frac{1}{n} \sum_{i=1}^{n} x_i \right] \times 100\ \% \tag{16}$$

where MBE is the mean bias error, $RMSE_{rel,no\ bias}$ is the relative root-mean-square error normalized by the mean of the measured values (also called the *coefficient of variation* of the root-mean-square error) with the mean bias error subtracted from the modeled values, n is the number of measurements, y_i is the ith modeled value, x_i is the ith measured value. The expanded uncertainty of this model for these test conditions can be calculated using the coefficient of variation of the root-mean-square error (*RMSE*) multiplied by a coverage factor:

$$U = k \sqrt{\frac{1}{n} \sum_{i=1}^{n} \left(y_i - x_i \right)^2} \div \left[\frac{1}{n} \sum_{i=1}^{n} x_i \right] \times 100\ \% \tag{17}$$

where k is the coverage factor, equal to 1.96 for a 95 % confidence level.

The results in Table 3 show that the augmented model affects the bias most notably right near the wall, where it marginally overpredicts the irradiance, as opposed to the HDKR model which underpredicts. The larger difference is in the root-mean-square error (with the bias removed), where the augmented model reduces this error for all measurement locations on the pitched roof, most so near the wall. The general overestimation by both models, indicated by the positive mean bias errors, can be reduced by assuming a lower ground albedo, which was originally estimated at 0.1. A value of 0.5 results in the bias errors for the augmented model to be lower than the HDKR for all locations except 1 and 2, which are near the edge of the reflector. This lower albedo value does not result in any change in the root-mean-square error (with the bias removed). The higher bias errors by the augmented model, predominantly near the edge of the reflector and using a ground albedo of 0.1, however, are only a maximum difference of 3.5 W/m^2, or 0.5% of the approximate midrange of the measured values (700 W/m^2), and therefore are relatively insignificant.

Overall, as shown in last column in Table 3, the uncertainty calculated for the measurements from all six locations, or the estimated model uncertainty for these test conditions, is 4.1 %, down 3.2 percentage points from 7.2 % when using the HDKR model. Note also that the HDKR model shows very good agreement with the measurements from the tilted pyranometer above the reflector.

Table 3
Modeling errors for both the HDKR model (assuming no wall) and the augmented model. Positive biases indicate model over-prediction; values in parentheses are the differences in the augmented model from the HDKR model, with differences in the absolute values given for the mean bias errors. The last two columns are the root-mean-square errors (*RMSE*) without the bias removed, multiplied by a coverage factor of 1.96.

	Mean Bias Error (*W/m*^{2})		*Root-Mean-Square Error* (bias removed) (%)		U_{95} (%)	
Location	HDKR Model	Augmented Model	HDKR Model	Augmented Model	HDKR Model	Augmented Model
1	5.8	6.5 (+|0.7|)	1.5	1.1 (-0.41)	3.2	2.6 (-0.60)
2	5.8	8.1 (+|2.3|)	2.2	1.4 (-0.83)	4.6	3.4 (-1.2)
3	-3.1	5.6 (+|2.5|)	5.4	2.9 (-2.5)	11	5.8 (-4.8)
4	3.3	3.2 (-|0.1|)	2.1	1.4 (-0.69)	4.1	2.8 (-1.3)
5	5.8	6.8 (+|1.0|)	3.1	1.8 (-1.3)	6.2	3.9 (-2.3)
6	-5.2	3.2 (-|2.0|)	5.3	2.4 (-2.9)	11	4.8 (-5.7)
Above Wall	-4.2	N/A	1.1	N/A	2.4	N/A
1-6	2.1	5.6 (+|3.5|)	3.7	1.9 (-1.7)	7.2	4.1 (-3.2)

A stepwise regression is performed on the residuals using various mostly independent measurements and related metrics to show unaccounted correlations in the model and indicate where it could be improved. This regression analysis starts with a simple linear regression using the predictor that results in the best fit, as quantified by the coefficient of determination (R^2). Additional predictors are added one at a time to this multiple regression, according to whichever one results in the largest increase in R^2. The variables included in this analysis include the solar azimuth and zenith angles, beam incidence angles on the collector and reflector, air mass, horizontal longwave radiation (IR), horizontal net-IR, diffuse fraction (ratio of horizontal diffuse to horizontal total irradiance), beam radiations on the collector and reflector, modeled diffuse and total irradiances on the reflector, and the case temperature of the pyrgeometer (which is likely very near to the case temperatures of the pyranometers).

Table 4 organizes the results of the stepwise regression in descending order of the incremental R^2 values for each measurement location. The first two or three variables listed for each location are therefore the ones having the highest correlations with the residuals and the ones least accounted for by the model.

The results in
Table 4 show that the irradiance on, and solar position relative to the reflector have the most effect on residual variance, but that there is also a large correlation with the IR radiation. The former could indicate that the irradiance modeling on the tilted reflector can be improved, and the latter that there is an unaccounted IR response in the pyranometers. This unaccounted response may simply be the known deviation between the IR measured on the horizontal roof above the reflector and the IR on the pitched collector.

Results specific to the HDKR model and respective measurements, corresponding to the location above the wall, show a significant correlation with case temperature, which is one of the largest typically unaccounted-for sources of uncertainty in pyranometer measurements (Reda, 2011).

4. Simulations

4.1. Sensitivity of the Model to Instantaneous Sky Clearness and Solar Position, and Collector and Reflector Configuration

The effect of a rear reflector on an equatorial-facing residential roof is evaluated using the model for representative values of the solar incidence angle, reflector albedo, reflector height, and collector pitch. One factor at a time is varied over a typical range, and the percent and absolute differences in collector irradiance are calculated versus sky clearness. The sky clearness is represented by the instantaneous clearness index k_T, which is the ratio of total horizontal irradiance to extraterrestrial radiation (the maximum possible irradiance). The diffuse horizontal irradiance is approximated using the Erbs et al. correlation (1982), which gives the diffuse fraction, or the ratio of diffuse horizontal to total horizontal irradiance, as a function of hourly clearness index. The beam normal radiation is back-calculated from the total horizontal irradiance (set by the clearness index) and the modeled diffuse horizontal irradiance.

Table 4
Results of a stepwise regression on the augmented model residuals (locations 1-6) and HDKR model residuals (location above the wall).

Location	Order	Variable	R^2	Inc. R^2
4	1	Horiz. IR	0.23	0.23
	2	Solar Azimuth Angle	0.33	0.11
	3	Beam Incidence Angle on Reflector	0.41	0.08
	4	Total Irradiance on Reflector	0.46	0.05
5	1	Solar Azimuth Angle	0.32	0.32
	2	Horiz. IR	0.40	0.07
	3	Beam Incidence Angle on Reflector	0.47	0.07
	4	Total Irradiance on Reflector	0.60	0.13
6	1	Beam Incidence Angle on Reflector	0.25	0.25
	2	Diffuse Irradiance on Reflector	0.53	0.28
	3	Beam Radiation on Collector	0.68	0.15
	4	Horiz. Net-IR	0.70	0.02
Above Wall	1	Temperature of Pyrgeometer	0.42	0.42
	2	Beam Radiation on Collector	0.61	0.19
	3	Solar Azimuth Angle	0.65	0.03
	4	Solar Zenith Angle	0.66	0.01

The typical ranges and representative parameters used in the model are:

- *solar altitude angles (α_s) of 2° to 88°, with a representative value of 50°*. This representative value is the complement of the approximate center latitude of the continental U.S. (39.8 °N), or the annual average solar altitude angle at solar noon. The solar azimuth is fixed at
- 0° (solar noon), when the solar altitude equals the beam incidence angle on the reflector.
- *reflector albedos (ρ_r) of 0.1 to 0.74, with a representative value equaling the average (0.42)*. This range is between the minimum and maximum values of typical building exterior walls and fenestrations (Reagan and Acklam, 1979), with a sample of materials and their albedos given in Table 5.
- *reflector heights (H_r) of 0 m to 5 m (0 ft to 16.4 ft), with a representative value of 2.13 m (7 ft)*. This representative value corresponds to a standard 2.44 m (8 ft) residential wall, factoring in an approximate 0.30 m (1 ft) floor assembly and an approximate 0.61 m. (2 ft) rise in the first story pitched roof.
- *collector pitches (β_c) of 0° to 45°, with a representative value of 26.6°*. This range spans between flat and 12:12 pitched roofs, and the representative value equals the pitch of a 6:12 roof.
- *collector center (x) 0.5 m to 2.5 m (1.6 ft to 8.2 ft) from the reflector, with a representative value of 1.5 m (4.9 ft)* (measured perpendicular to reflector in collector plane), away from the edge of the reflector
- *collector width of 1 m (3.28 ft)* (measured perpendicular to reflector in collector plane)
- *ground albedo (ρ_g) of 0.1*.

Table 5
A sample of typical exterior building surface albedos.

Exterior Building Material	Albedo (ρ)
White Paint[1]	0.55 to 0.74
Beige Paint[1]	0.26 to 0.55
Colored Slump Block, CMU, Bricks[1]	0.21 to 0.51
Low-Emissivity (Low-E) Windows[2]	0.33
Brown Stained Wood[1]	0.10 to 0.13
Standard Windows[2]	0.08

[1] Reagan and Acklam, 1979

[2] Anello et al., 2000. The reflectivities of windows are given, but they are not true albedos as they exhibit high specular reflectivity, and therefore are not accurately modeled here.

The results of these simulations are shown in Figure 5; note that the clearness index is rarely above 0.9 (Erbs et al., 1982). The model shows that the reflector reduces the irradiance during cloudy periods and increases the irradiance during sunny periods, more so at lower solar altitude (reflector incidence) angles. As expected, an increase in reflector albedo increases the collector irradiance by increasing the reflected radiation.

The relationship between the height of the reflector, the pitch of the collector, and the distance between the collector and reflector and how they relate to the view factor between the collector and reflector are apparent in Figure 5c, d, and e. An increase in reflector height is shown to have a negative effect during cloudy periods and a positive effect during clear periods. During cloudy periods the reflector is blocking diffuse irradiance that is a larger fraction of the total than it is reflecting during sunny periods; however, the absolute value of the reflected irradiance is one and a half times that of the blocked diffuse (65 W/m^2 versus -40 W/m^2). A lower collector pitch and a closer collector location to the reflector increases the view angle with the collector and allows it to intercept more of the reflected radiation, but it also reduces its view to the available sky not blocked by the reflector, which causes a decrease in irradiance during cloudy periods.

The effect of the reflector on the collector irradiance is therefore a balance between the increased irradiance from the reflections and the decreased diffuse irradiance from the fraction being blocked by the other side of the reflector. Below a clearness index of approximately 0.55, the reflector reduces the irradiance on the collector nearly irrespective of the other variables, and above that index value it augments the irradiance. Although this outcome is not accounted for in the model, the reflector will also block some direct normal irradiance from the collector when the sun is behind the reflector in the morning and evening (for an equatorial facing configuration), but these periods will be times of low irradiance, especially on a pitched collector.

4.2. Effect on Annual Insolation

The annual effect of an adjacent equatorial-facing planar vertical diffuse reflector on pitched collector insolation is calculated for eight U.S. cities, one in each of the eight different climate zones specified by the 2012 International Energy Conservation Code (IECC) (ICC, 2011). The chosen cities are ones with large populations, the highest class of third-set Typical Meteorological Year (TMY3) data that is available in the zone, and latitudes that result in a relatively even distribution across the continental U.S., plus Alaska. The annual results are split into two equal six month time frames between April and September (summer) and October and March (winter). The effects of sky clearness and incidence angle distributions are shown by the simulation results for different climate zones, and latitudes and times of the year, respectively. Results from this city data, however, may not be consistent for the entire respective climate zone.

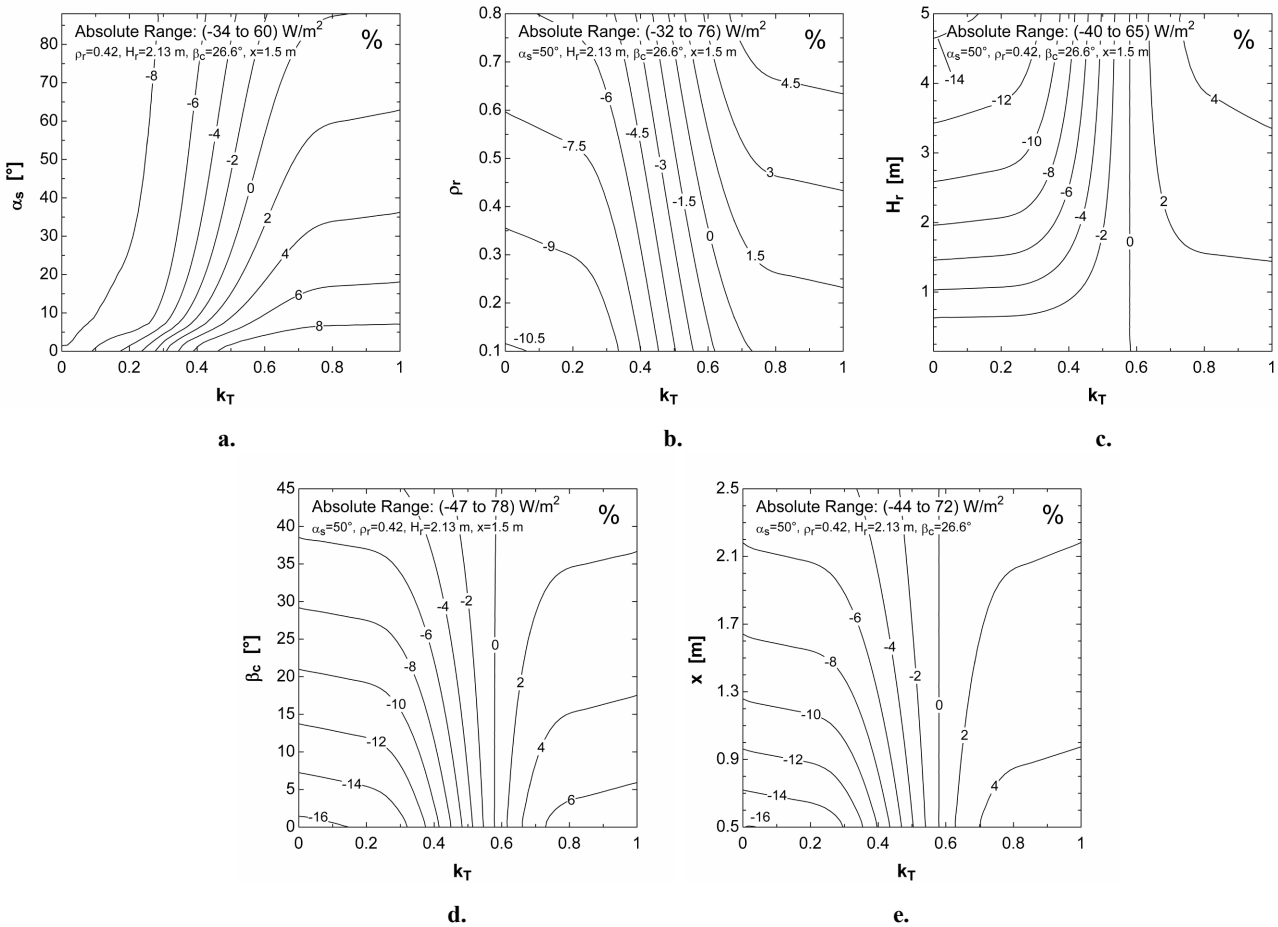

Figure 5: Modeled relative and absolute differences between collector irradiance with and without a rear vertical diffuse reflector, versus clearness index, for typical ranges and representative values of (a) solar altitude angles at solar noon, (b) reflector albedos, (c) reflector heights, (d) collector pitches, and (e) distance from collector center to reflector.

Model simulations use hourly insolation data from the TMY3 data sets and the following inputs:

- reflector albedos of 0.1 and 0.74
- reflector height of 2.13 m (7 ft)
- collector pitches of 0°, 26.6° (6:12), and 45° (12:12)
- collector center 0.5, 1.5, and 2.5 m (1.6-8.2 ft) from the reflector, away from the edge of the reflector
- collector width of 1 m (3.28 ft) (measured perpendicular to reflector in collector plane)
- ground albedo of 0.1

The beam and circumsolar insolations are also set to zero during the hours at which the solar azimuth angle is greater than ±90° (behind the reflector), as calculated at the midpoint of the hour. The results of this analysis are given in Figure 6. Care should be taken when applying these results as model validation occurred for only the months of April through June.

The analysis shows that vertical diffuse reflectors almost always result in a decrease in insolation in the summer months and, for higher than average reflector albedos, an increase in the winter months. In the summer, when the insolation on a vertical surface is lower due to higher solar altitude angles, the reflected insolation is less than the diffuse and morning and evening direct insolation that the reflectors block. In the winter, the sun is at a lower altitude, and more insolation is incident on and reflected by the reflectors. In only optimal configurations, when the collector is close to the reflector and the reflector albedo is high,

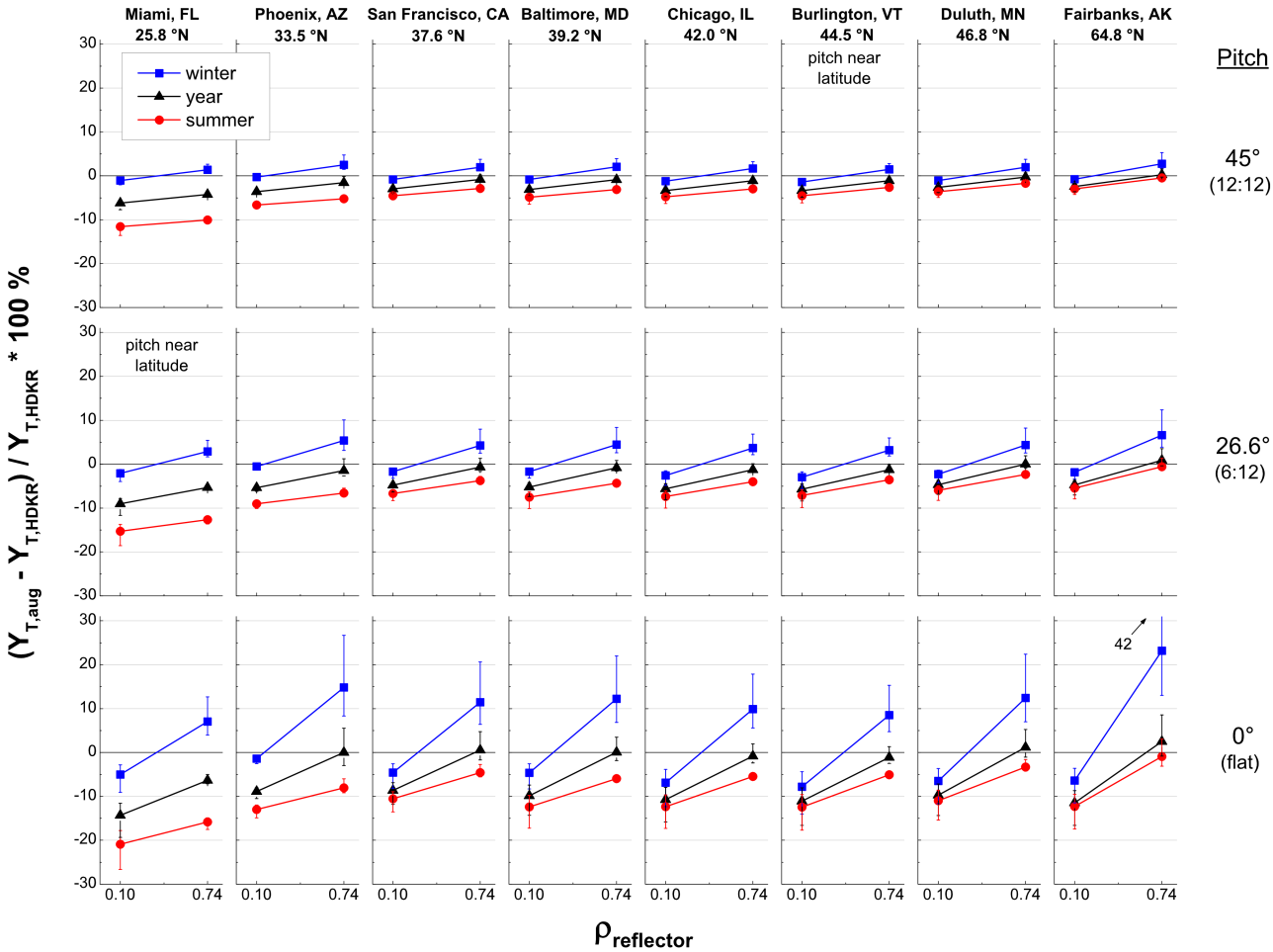

Figure 6: Modeled differences in seasonal and annual insolations for eight U.S. cities in separate climate zones as a function of collector pitch and reflector albedo. Error bars show effect of moving the collector closer or farther from the reflector; higher annual insolations are experienced by collectors nearer to high albedo reflectors and farther from low albedo reflectors.

will the reflector result in a net increase in annual collector insolation. This is shown in Figure 6 by the lines and error bars for yearly predictions that extend above the zero mark, noting that positive error bars correspond to collectors nearer to high albedo reflectors and farther from low albedo reflectors.

For all cities, although not differentiated in the figure, higher annual insolations are experienced by collectors nearer to high albedo reflectors, while for lower albedo reflectors, higher annual insolations are experienced by collectors farther from the reflectors. This finding is consistent for both summer and winter insolations, except in the summer in Miami where higher insolations are experienced for collectors farther from the reflectors, regardless of the reflector albedo. High albedo reflectors reflect more insolation onto close collectors than the diffuse irradiance they block, while low albedo reflectors are blocking more insolation than they are reflecting. In low latitude locations like Miami, the sun is higher in the summer sky and less insolation is incident on the vertical reflector, thereby critically reducing the magnitude of the reflections.

A reflector is also shown to reduce summer insolation for these low latitude locations with predominately clear skies, which includes Miami and Phoenix. At these locations, where the sun is in the north half of the sky a greater percentage of the time and more of the insolation is direct, 6 % to 17 % of the summer insolation is blocked by the reflector, compared to 2 % to 8 % for the other locations (not shown in the figure).

The results show that higher annual insolations are experienced by lower pitched collectors near high albedo reflectors, while for lower albedo reflectors, higher annual insolations are experienced by higher pitched collectors. More reflected insolation is intercepted by lower pitched collectors, due to the higher view factor between the collector and reflector. However, if the reflector is blocking more diffuse insolation than it is reflecting, as is the case for lower albedo reflectors, a higher pitched collector will intercept

more of the insolation directly from the sun and the viewable sky.

The effects of the reflectors are also shown to have less annual variability for higher latitudes and steeper pitches. At higher latitudes there are lower differences in the cosine of the solar incidence angles on the reflector resulting in a more constant amount of reflected insolation. For steeper pitches there is a lower view angle between the collectors and reflectors resulting in a lower absolute and therefore consistently lower relative effect.

Overall, the results of this analysis are conservative, or underpredict the insolation, because the beam and circumsolar radiations are not zero for all areas on the roof when the sun is behind the reflector, as is how it is modeled. However, in the case of photovoltaic (PV) solar technologies, it may be closer to the actual utilizable irradiance, due to their extreme sensitivity to partial shading (Deline, 2009; Sera and Baghzouz, 2008). The results will also change for installation-specific parameters different than the representative values modeled in this study, including the proximity of the collector to the edge of the reflector and the reflector height. Another factor that should be considered is that low-pitched collectors, although intercepting more reflected irradiance, will accumulate more soiling that will offset some of the benefit.

5. Conclusions

The planar vertical diffuse reflector irradiance model presented here indicates that collector irradiance is sensitive to sky clearness, solar position, and numerous variables associated with the collector and reflector configuration. The model is in good agreement with the measured data from the test bed used in this research, reducing the modeled uncertainty more than three percentage points relative to the HDKR model. The model does not account for shading of direct solar radiation by the reflector, which is more prevalent for larger reflectors, reflectors at higher latitudes, reflectors not facing the equator, or for configuration having smaller angles between the reflector and collector. Specular reflections and inter-reflections between multiple diffuse reflectors must also be considered separate from this model.

The model indicates that a reflector can increase collector irradiance by up to 8 % for an optimized, yet typical, configuration during clear sky conditions and low reflector incidence angles, while decreasing the irradiance by up to 16 % during cloudy sky conditions and high, or glancing, reflector incidence angles, as shown in Figure 5. For a typical year in various U.S. climate zones, the presence of a reflector will result in annual collector insolation differences between -19 % and 9 %. An increase in annual insolation is possible for nearly all climate zone locations if the collector is adjacent to a very high albedo reflector.

This research shows that lower roofs with a reflective rear wall can provide additional space to mount solar collectors without sacrificing output, and in some cases, increase the output. Rear reflecting walls will also moderately shift the seasonal insolation from the summer to the winter, which may be advantageous for solar thermal collectors.

Acknowledgements

The author would like to thank Stacy Bruss and Keith Martin at the NIST library for conducting numerous and thorough literature reviews in support of this work. The assistance of Luis Luyo and Philip Weinstein at the NIST Engineering Laboratory with fabricating the instrument mounts is also much appreciated. The author also gratefully acknowledges the expert guidance of Ibrahim Reda at NREL with respect to pyranometer calibrations.

References

Anello, M.T., Parker, D.S., Sherwin, J.R., Richards, K., 2000. Measured impact of advanced windows on cooling energy use, in: Proceedings of the ACEEE 2000 Summer Study on Energy Efficiency in Buildings.

Bollentin, J.W., Wilk, R.D., 1995. Modeling the solar irradiation on flat plate collectors augmented with planar reflectors. Solar Energy 55, 343–354.

Chiam, H.F., 1981. Planar concentrators for flat-plate solar collectors. Solar Energy 26, 503–509.

Chiam, H.F., 1982. Stationary reflector-augmented flat-plate collectors. Solar Energy 29, 65–69.

Crawley, D.B., Lawrie, L.K., Pedersen, C.O., Winkelmann, F.C., 2000. Energy plus: energy simulation program. ASHRAE journal 42, 49–56.

Deline, C., 2009. Partially shaded operation of a grid-tied PV system. Presented at the Photovoltaic Specialists Conference (PVSC), 2009 34th IEEE, pp. 1268–1273.

Duc Hien, V., Chirarattananon, S., 2009. An experimental study of a facade mounted light pipe. Lighting Research and Technology 41, 123–142.

Duffie, J.A., Beckman, W.A., 2006. Solar Engineering of Thermal Processes, 3rd ed. John Wiley & Sons, Inc., Hoboken, NJ.

Erbs, D.G., Klein, S.A., Duffie, J.A., 1982. Estimation of the diffuse radiation fraction for hourly, daily and monthly-average global radiation. Solar Energy 28, 293–302.

Grassie, S.L., Sheridan, N.R., 1977. The use of planar reflectors for increasing the energy yield of flat-plate collectors. Solar Energy 19, 663–668.

Grimmer, D.P., Zinn, K.G., Herr, K.C., Wood, B.E., 1978. Augmented solar energy collection using different types of planar reflective surfaces; theoretical calculations and experimental results. Solar Energy 21, 497–501.

Gueymard, C.A., 2009. Direct and indirect uncertainties in the prediction of tilted irradiance for solar engineering applications. Solar Energy 83, 432–444.

Hansen, F.V., 1993. Albedos (No. ARL-TR-57). Army Research Laboratory.

Hein, V.D., Chirarattananon, S., 2005. Triangular subdivision for the computation of form factors. LEUKOS, The Journal of the Illuminating Engineering Society of North America 2, 41–60.

Howell, J.R., 2012. A Catalog of Radiation Heat Transfer Configuration Factors, Equation C-17 [WWW Document]. URL http://www.me.utexas.edu/~Howell/tablecon.html

International Code Council (ICC), 2011. International Energy Conservation Code (IECC) (2012).

International Organization for Standardization (ISO), 1992. Solar energy - Calibration of field pyranometers by comparison to a reference pyranometer (Standard No. 9847:1992(E)). Geneva.

JCGM/WG 1, 2010. Evaluation of measurement data - Guide to the expression of uncertainty in measurement (100:2008). Working Group 1 of the Joint Committe for Guides in Metrology.

Kipp and Zonen, 2008. CHP 1 Pyrheliometer Instruction Manual.

Klein, S.A., 2012. Engineering Equation Solver (EES). F-Chart Software.

Larson, D.C., 1979. Mirror enclosures for double-exposure solar collectors. Solar Energy 23, 517–524.

Larson, D.C., 1980. Optimization of flat-plate collector-flat mirror systems. Solar Energy 24, 203–207.

Lauzier, N., 2004. View Factors [WWW Document]. File Exchange - MATLAB Central. URL http://www.mathworks.com/matlabcentral/fileexchange/5664-view-factors

Loutzenhiser, P.G., Manz, H., Felsmann, C., Strachan, P.A., Frank, T., Maxwell, G.M., 2007. Empirical validation of models to compute solar irradiance on inclined surfaces for building energy simulation. Solar Energy 81, 254–267.

MATLAB, 2010. The Mathworks Inc., Natick, MA.

McDaniels, D.K., Lowndes, D.H., Mathew, H., Reynolds, J., Gray, R., 1975. Enhanced solar energy collection using reflector-solar thermal collector combinations. Solar Energy 17, 277–283.

Myers, D.R., Stoffel, T.L., Reda, I., Wilcox, S.M., Andreas, A.M., 2002. Recent Progress in Reducing the Uncertainty in and Improving Pyranometer Calibrations. Journal of Solar Energy Engineering 124, 44.

NIST/SEMATECH, 2012. e-Handbook of Statistical Methods [WWW Document]. URL http://www.itl.nist.gov/div898/handbook/

Oren, M., Nayar, S.K., 1994. Generalization of Lambert's Reflectance Model. Presented at the ACM 21st Annual Conference on Computer Graphics and Interactive Techniques (SIGGRAPH), pp. 239–246.

Padovan, A., Del Col, D., 2010. Measurement and modeling of solar irradiance components on horizontal and tilted planes. Solar Energy 84, 2068–2084.

Pelletier, G., 2005. Sunrise/Sunset. URL http://www.ecy.wa.gov/programs/eap/models.html

Perers, B., Karlsson, B., 1993. External reflectors for large solar collector arrays, simulation model and experimental results. Solar Energy 51, 327–337.

Reagan, J.A., Acklam, D.M., 1979. Solar reflectivity of common building materials and its influence on the roof heat gain of typical southwestern U.S.A. residences. Energy and Buildings 2, 237–248.

Reda, I., 2011. Method to calculate uncertainties in measuring shortwave solar irradiance using thermopile and semiconductor solar radiometers (Technical Report No. NREL/TP-3B10-52194). National Renewable Energy Laboratory (NREL).

Reindl, D.T., Beckman, W.A., Duffie, J.A., 1990. Evaluation of hourly tilted surface radiation models. Solar Energy 45, 9–17.

Sera, D., Baghzouz, Y., 2008. On the impact of partial shading on PV output power. Presented at the 2nd WSEAS/IASME International Conference on Renewable Energy Sources.

Stein, J.S. et al. 2010. A standardized approach to PV system performance model validation, in: Proc. 35th IEEE PVSC. Hawaii, USA.

US Department of Energy, 2012. EnergyPlus-Engineering reference.

Winkelmann, F.C., 1983. Daylighting calculation in DOE-2, in: DOE-2 Engineers Manual. U.S. Department of Energy, pp. 700–763.

Winkelmann, F.C., Birdsall, B.E., Buhl, W.F., Ellington, K.L., Erdem, A.E., Hirsch, J.J., Gates, S., 1993. DOE2 Supplement, Version 2.1E (Technical Report No. LBL-34947). Lawrence Berkeley National Laboratory, Springfield, Virginia: National Technical Information Service.